frontiers in Chemistry

ORIGINAL RESEARCH
published: 01 March 2018
doi: 10.3389/fchem.2018.00037

Ti_4O_7/g-C_3N_4 Visible Light Photocatalytic Performance on Hypophosphite Oxidation: Effect of Annealing Temperature

Wei Guan[1], *Gaoge Sun*[2], *Lei Yin*[3], *Zhenghua Zhang*[4*†] *and Shichao Tian*[5*†]

[1] Chongqing Key Laboratory of Environmental Materials and Remediation Technologies, Chongqing University of Arts and Sciences, Chongqing, China, [2] Department of Chemistry, Tsinghua University, Beijing, China, [3] Heibei Yinfa Meifute Environmental Engineering Co., Ltd., Shijiazhuang, China, [4] Research Institute of Environmental Engineering and Nano-Technology, Graduate School at Shenzhen, Tsinghua University, Shenzhen, China, [5] Shenzhen Environmental Science and New Energy Technology Engineering Laboratory, Tsinghua-Berkeley Shenzhen Institute, Shenzhen, China

OPEN ACCESS

Edited by:
Fan Dong,
Chongqing Technology and Business University, China

Reviewed by:
Hongwei Huang,
China University of Geosciences, China
Michael Nolan,
University College Cork, Ireland

***Correspondence:**
Zhenghua Zhang
zhenghua.zhang@sz.tsinghua.edu.cn
Shichao Tian
18812672619@163.com

[†] These authors have contributed equally to this work.

Specialty section:
This article was submitted to Catalysis and Photocatalysis, a section of the journal Frontiers in Chemistry

Received: 04 December 2017
Accepted: 14 February 2018
Published: 01 March 2018

Citation:
Guan W, Sun G, Yin L, Zhang Z and Tian S (2018) Ti_4O_7/g-C_3N_4 Visible Light Photocatalytic Performance on Hypophosphite Oxidation: Effect of Annealing Temperature. Front. Chem. 6:37. doi: 10.3389/fchem.2018.00037

The oxidation of hypophosphite to phosphate is the key to recover the phosphorus resource from the hypophosphite wastewater. In the present work, Ti_4O_7/g-C_3N_4 composites were synthesized at two different temperatures (100 and 160°C) and their performance on photocatalytic oxidation of hypophosphite under visible light irradiation and the corresponding mechanism were evaluated. A hydrolysis method using g-C_3N_4 and Ti_4O_7 was applied to synthesize the Ti_4O_7/g-C_3N_4 composites with their hybrid structure and morphology confirmed by X-ray diffraction (XRD), scanning electron microscopy (SEM), and X-ray photoelectron spectra (XPS). The annealing temperature significantly affected the photocatalytic performance of Ti_4O_7/g-C_3N_4 that the 160-Ti_4O_7/g-C_3N_4 composite (fabricated at 160°C) showed the highest oxidation efficiency of hypophosphite of 81% and the highest photocatalytic oxidation rate of 0.467 h^{-1} comparing with the 100-Ti_4O_7/g-C_3N_4 composite (fabricated at 100°C) and pure g-C_3N_4. The enhanced photocatalytic performance of 160-Ti_4O_7/g-C_3N_4 could be ascribed to the effective charge separation and enhanced photoabsorption efficiency. Additionally, electron spin resonance (ESR) results showed that hydroxyl radicals and superoxide anion radicals were mainly responsible to the oxidation of hypophosphite with superoxide anion radicals accounting for a more significant contribution. Moreover, Ti_4O_7/g-C_3N_4 photocatalysts showed the remarkable stability in the repetitive experiments.

Keywords: graphitic carbon nitride, sub-stoichiometric titanium oxides, hypophosphite, hydroxyl radicals, superoxide anion radicals

INTRODUCTION

Hypophosphite is commonly used as a reducing agent in metallurgy industries especially in the processes of plating and surface finishing thereby generating large amounts of hypophosphite wastewater (Bulasara et al., 2011; Li et al., 2015). The hypophosphite contaminant should be further treated before being discharged into the river or lake, because it may lead to algae growth

and cause eutrophication (Wang et al., 2016; Ge et al., 2017). In addition, phosphorus is a non-renewable resource mainly used as a nutrient in agricultural production (Montangero and Belevi, 2007). Due to an increase in the global demand for phosphorus resource, it will be depleted in the next 50–100 years (Takeda et al., 2010; Ye Y. Y. et al., 2017; Ye Z. L. et al., 2017). Therefore, the phosphorus recovery from wastewater is of considerable interest. However, a high solubility constant of the hypophosphite precipitants limits the transformation of hypophosphite into the precipitated products. In contrast, phosphate is easier to be recovered than hypophosphite by precipitation. As such, a highly efficient approach for the pre-oxidation of hypophosphite to phosphate becomes of great importance for phosphorus recovery. Photocatalysis, a nano-enabled technology, has been recognized for its promising applications with the generation of activated radicals such as hydroxyl radicals and superoxide anion radicals, which herein can be applied for hypophosphite oxidation.

Semiconductor photocatalysts have been recognized as a potential strategy to solve some serious challenges of the twenty-first century, such as energy shortage, environmental pollution, and global warming (Lin et al., 2017). TiO_2 photocatalyst has attracted much attention due to its strong oxidizing power, low cost and high chemical stability. However, a large band gap (3.2 eV) of TiO_2 means that it can only absorb ultraviolet light (only about 3–5% of total sunlight), which greatly limits its performance in industrial applications (Teng et al., 2017; Noman et al., 2018). Therefore, it is urgent to develop novel semiconductor photocatalysts that respond to visible light.

Recently, graphitic carbon nitride (g-C_3N_4), constituted by numerous layers of two-dimensional (2D) counterparts, has attracted enormous attention given its advantages such as low cost and visible light driven semiconductor photocatalyst (Huang et al., 2017b; Liu et al., 2017a,b; Tian et al., 2017; Wang et al., 2017). The metal free g-C_3N_4 can work as photocatalyst under visible light irradiation with a suitable band gap of 2.7 eV. In addition, g-C_3N_4 possesses excellently structural stability, which is suitable for chemical modification. Nevertheless, the photocatalytic property of g-C_3N_4 is still limited for its low surface area, low photoabsorption efficiency and high recombination rate of photo-induced electron-hole pairs (Jourshabani et al., 2017; Shao et al., 2017).

Decreasing the recombination of photo-induced carriers during the photocatalytic process would enhance the photocatalytic activity of the as-prepared g-C_3N_4 photocatalyst (Li J. D. et al., 2017). Therefore, some methods, such as porosity engineering, doping with foreign elements, and compositing with other semiconductors to facilitate charge separation, were developed to enhance the photocatalytic performance of g-C_3N_4. For example, the horn-like hollow mesoporous ultrathin g-C_3N_4 tubes were fabricated with high surface area, drastically boosted bulk charge separation, carrier density and surface charge transfer efficiency and showed the remarkably photocatalytic performance for H_2 evolution (Liu et al., 2017a). Meanwhile, the 3D mesoporous g-C_3N_4 established by ultrathin self-doped nanosheets exhibited the superior photocatalytic performance on hydrogen evolution (Tian et al., 2017). Additionally, the porous and thin g-C_3N_4 nanosheets, prepared via a novel thiourea-assisted melamine-precursor hydrothermal pre-treatment followed by a traditional thermal polymerization method, profoundly enhanced visible-light photocatalytic performance on H_2 evolution and NO removal from the gaseous phase (Huang et al., 2017b). Moreover, the Cl intercalated mesoporous g-C_3N_4 showed outstanding photocatalytic performance for water splitting into H_2, CO_2 reduction, liquid and air contaminants removal (Liu et al., 2017b).

Substoichiometric titanium oxides, known as Magnéli phases (Sun et al., 2016), comprise a series of compounds with the generic formula Ti_nO_{2n-1} ($4 \leq n \leq 10$) (Kolbrecka and Przyluski, 1994; Guo et al., 2016). Among these compounds, Ti_4O_7 possesses high electrical conductivity, thermal stability, and corrosion resistance in harsh conditions (Oturan et al., 2017). Therefore, Ti_4O_7 is wildly used as catalyst coated material (Li et al., 2010), wastewater treatment material (You et al., 2016), support material in fuel cell (Chisaka et al., 2016), and additive to positive materials in batteries (Cao et al., 2017). However, it was also reported that pure Ti_4O_7 as the photocatalyst had limited photocatalytic activity with the band gap of 2.9 eV (Maragatha et al., 2017). Herein, coupling Ti_4O_7 and intrinsic g-C_3N_4 to construct the well-matched Ti_4O_7/g-C_3N_4 heterojunction would be an alternative novel pathway to address the intrinsic drawbacks of g-C_3N_4 for photocatalytic applications.

In this study, novel Ti_4O_7/g-C_3N_4 photocatalysts were synthesized at two different temperatures (100 and 160°C) and their performance in photocatalytic oxidation of hypophosphite under visible light irradiation and the corresponding mechanism were compared and investigated. Ti_4O_7/g-C_3N_4 photocatalysts exhibited an enhanced photocatalytic activity for hypophosphite oxidation under visible light irradiation and the annealing temperature significantly affected the photocatalytic performance. The separation mechanism of photogenerated electrons and holes of the photocatalysts was investigated by UV-Vis diffuse reflectance spectra, photoluminescence emission spectra, cyclic voltammetry (CV), and electrochemical impedance spectroscopy (EIS). The activated species generated in the photocatalytic process were measured by electron spin resonance (ESR). The enhanced photocatalytic performance could be ascribed to the efficient charge separation and transfer across the heterojunction interface and the enhanced photoabsorption efficiency. Our work demonstrated that the rational design and construction of isotype heterojunction was an effective strategy for the development of efficient photocatalysts under visible light irradiation.

MATERIALS AND METHODS

Chemicals

Melamine ($C_3H_6N_6$), urea [$CO(NH_2)_2$], sub-stoichiometric titanium oxide (Ti_4O_7), sodium hypophosphite (NaH_2PO_2), sodium sulfate (Na_2SO_4), isopropanol [IPA, $(CH_3)_2CHOH$], ethylenediaminetetraacetic acid disodium salt ($C_{10}H_{14}N_2Na_2O_8$), sodium hydroxide (NaOH), and sulfuric acid (H_2SO_4) were provided by Sinopharm Chemical Reagent Co., Ltd. (Beijing, China). 5,5-dimethylpyrroline-N-oxide (DMPO)

was bought from Dojindo Co., Ltd. (Shanghai, China). The entire chemical reagents were analytical grade and all solutions were prepared using Milli-Q water (Millipore, 18.2 MΩ cm).

Synthesis of g-C_3N_4 Materials

The g-C_3N_4 materials were prepared using a liquid-based growth method (Sun et al., 2018). In a typical process, the mixture of melamine and urea (molar ratio = 1:1) was dissolved with 50 mL deionized water and then vigorously stirred for 1 h at room temperature. After that, the mixture suspension was centrifuged at 7,500 r/min for 15 min, and then dried at 60°C for 24 h under the vacuum to obtain the white powder. After that, the prepared white powders were further grinded into smaller powders in a mortar and placed in a muffle furnace. The powders were then annealed at 550°C in a muffle furnace for 4 h in static air at a ramp rate of 2.5°C min^{-1}. The resulting yellow products were collected for further usage.

Preparation of $Ti_4O_7/g\text{-}C_3N_4$ Photocatalysts

The preparation procedure of $Ti_4O_7/g\text{-}C_3N_4$ photocatalysts was shown below: g-C_3N_4 powder (2.0 g) and Ti_4O_7 (1.0 g) were dispersed into 100 mL NaOH (0.1 mol/L) by ultrasonication for 0.5 h. Subsequently, the mixed liquor was transferred to reaction still and then annealed in different temperatures (100 and 160°C) for 20 h. After that, the obtained precipitates were collected by centrifugation and washed with distilled water, and then dried at 60°C for 12 h. Samples fabricated at different annealing temperatures were noted as 100-$Ti_4O_7/g\text{-}C_3N_4$ (fabricated at 100°C) and 160-$Ti_4O_7/g\text{-}C_3N_4$ (fabricated at 160°C), respectively.

Samples Characterization

The concentration of NaH_2PO_2 was measured by ion chromatography using a 732 IC detector (McDowell et al., 2004). The crystal phase composition and fineness of the samples were analyzed by X-ray diffraction (XRD) with Cu Kα radiation in the scanning range of 2θ = 5–80° (model D/max RA, Rigaku Co., Japan). The surface morphology of the as-developed samples was examined by scanning electron microscopy (SEM) (JEOL JSM-6701F). The valence state of the deposition was measured by X-ray photoelectron spectra (XPS) (PHI-5300/ESCA, ULVAC-PHI, INC). The UV–vis diffuse reflection spectra (UV–vis DRS) of the samples was obtained by a UV–vis spectrophotometer (UV-2450, Shimadzu, Japan). Electrochemical properties of the $Ti_4O_7/g\text{-}C_3N_4$ and g-C_3N_4 photocatalysts, including photocurrents (PC), CV, and EIS, were measured on a CHI 660B electrochemical system. Electron spin resonance (ESR) (ESRA-300, Bruker, Germany) signals were recorded by the probe molecular 5,5-dimethyl-1-pyrroline-N-oxide (DMPO) to identify the radicals generated under visible light irradiation (λ > 420 nm) (Tian et al., 2015).

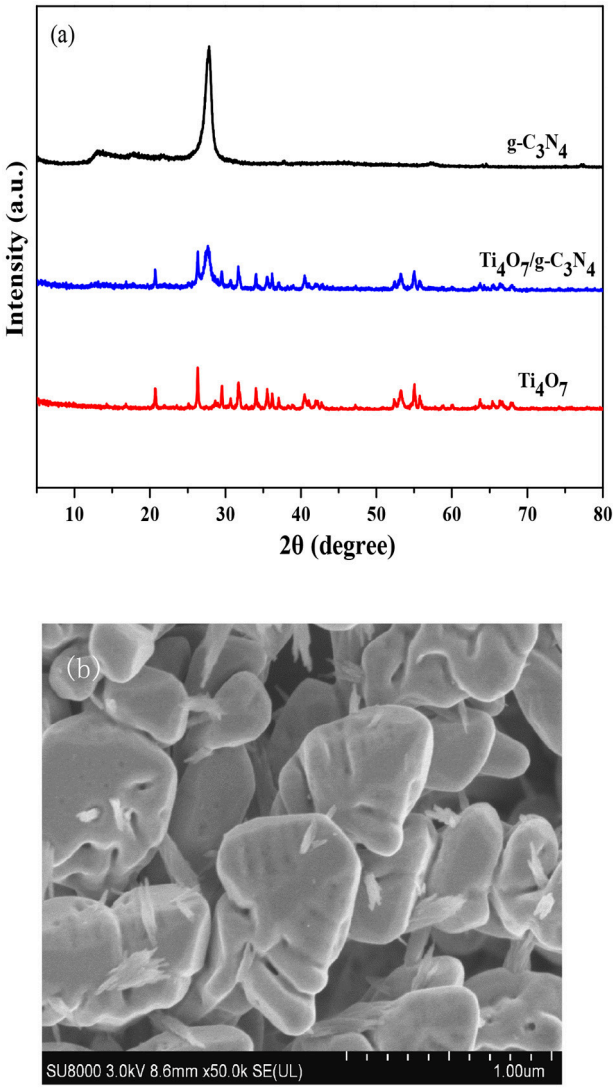

FIGURE 1 | Structure and morphology analyses. **(a)** XRD patterns of the g-C_3N_4, Ti_4O_7 and 160-$Ti_4O_7/g\text{-}C_3N_4$ photocatalysts; **(b)** SEM image of the 160-$Ti_4O_7/g\text{-}C_3N_4$ photocatalyst.

Evaluation of Photocatalytic Activity

The photocatalytic activities of as-synthesized samples were evaluated by the oxidation of hypophosphite in aqueous solution under visible light irradiation. For hypophosphite oxidation, the light source was a 35 W metal-halide lamp (Philips) with a 420 nm UV-cutoff filter. The lamps were located 12 cm away from the surface of reaction solution (about 5 mW cm^{-2}). In each experiment, photocatalyst (10 mg) was dispersed in hypophosphite (100 ml, 100 mg L^{-1}) aqueous solution. Before irradiation, the solution was continuously stirred in the dark for 2 h to reach adsorption-desorption equilibrium between the hypophosphite and the photocatalyst. During the photocatalytic reaction, the solutions were kept magnetically stirring, and 4 ml mixture was collected at 1 h intervals followed by centrifugation (10,000 rpm, 5 min) to remove the photocatalyst.

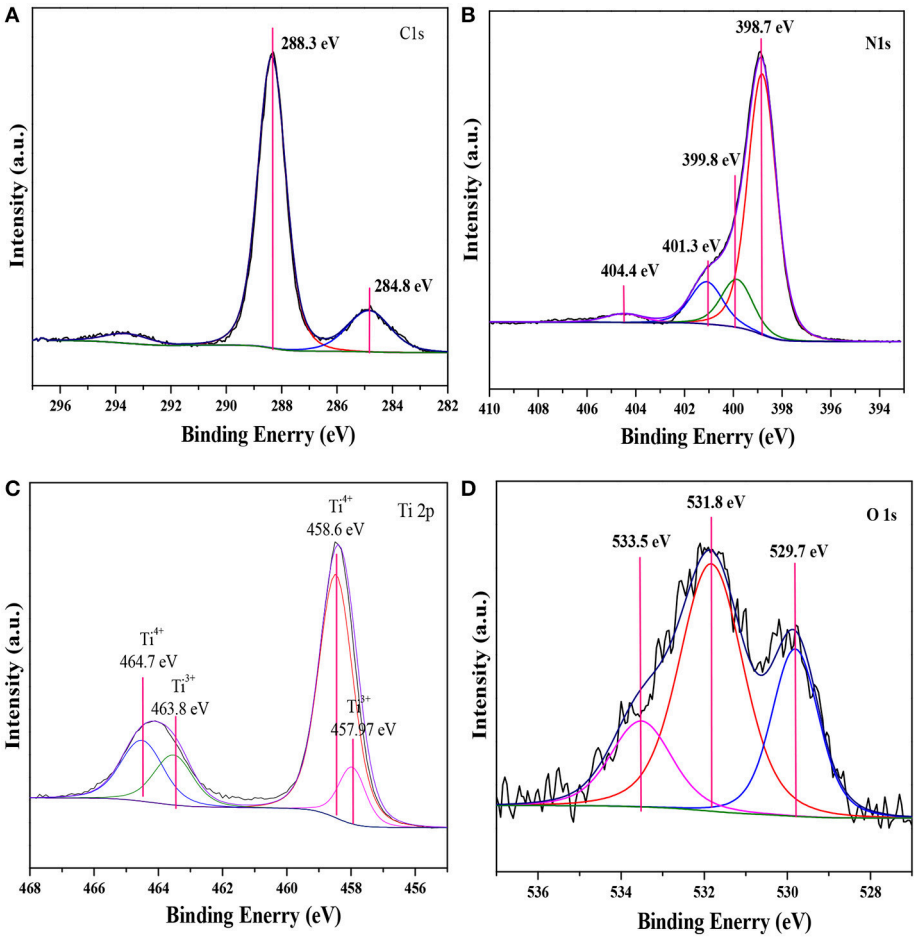

FIGURE 2 | XPS spectra of the 160-Ti_4O_7/g-C_3N_4 photocatalyst. **(A)** C 1 s; **(B)** N 1 s; **(C)** Ti 2 p; **(D)** O 1 s.

Radicals Quencher Experiment for Photocatalysis

In order to identify the contributions of the radicals generated in the photocatalytic oxidation process, IPA and N_2 purging were applied with IPA acting as the ·OH radicals quencher and N_2 purging reducing the superoxide $\cdot O_2^-$ radicals (Yang et al., 2016). Adding different radical scavengers into reaction solutions would affect the photocatalytic performance. As such, the contributions of ·OH radicals and $\cdot O_2^-$ radicals on photocatalytic oxidation of hypophosphite under visible light irradiation can be evaluated based on the change of photocatalytic oxidation efficiency of hypophosphite with and without IPA (1 mM) and N_2 purging (continuous purging).

RESULTS AND DISCUSSION

Structure and Morphology Analyses

The crystal structures of g-C_3N_4, Ti_4O_7, and 160-Ti_4O_7/g-C_3N_4 photocatalysts were characterized by XRD. As shown in **Figure 1a**, two pronounced diffraction peaks in pure g-C_3N_4 were observed at 13.20° and 27.60°, respectively. The peak at 13.20° was corresponded to (1 0 0) plane of tri-s-triazine units (Zhang et al., 2012a). The peak at 27.60°indexed as (0 0 2) peak was due to the interlayer-stacking of aromatic systems as in graphite (Zhang et al., 2012b). The characteristic peaks of Ti_4O_7 were matched well with the standard card (JCPDF 50-0787). The main diffraction peaks of 160-Ti_4O_7/g-C_3N_4 photocatalyst did not change obviously, indicating that the fabrication process did not destroy the main structure of both counterparts. The microstructure of the 160-Ti_4O_7/g-C_3N_4 photocatalyst was shown in **Figure 1b**. It was mainly composed of spheroidal crystals, and the shape of synthesized 160-Ti_4O_7/g-C_3N_4 photocatalyst was relatively uniform.

XPS measurements were carried out to investigate the compositions and elemental chemical states of the samples. As shown in **Figure 2**, the XPS spectra revealed that the elements of C, N, Ti and O existed on the surface of 160-Ti_4O_7/g-C_3N_4 photocatalyst. The corresponding high resolution spectra of C 1s, N 1s, Ti 2p, and O 1s were also analyzed. The XPS spectra of C 1s core level for 160-Ti_4O_7/g-C_3N_4 photocatalyst was shown

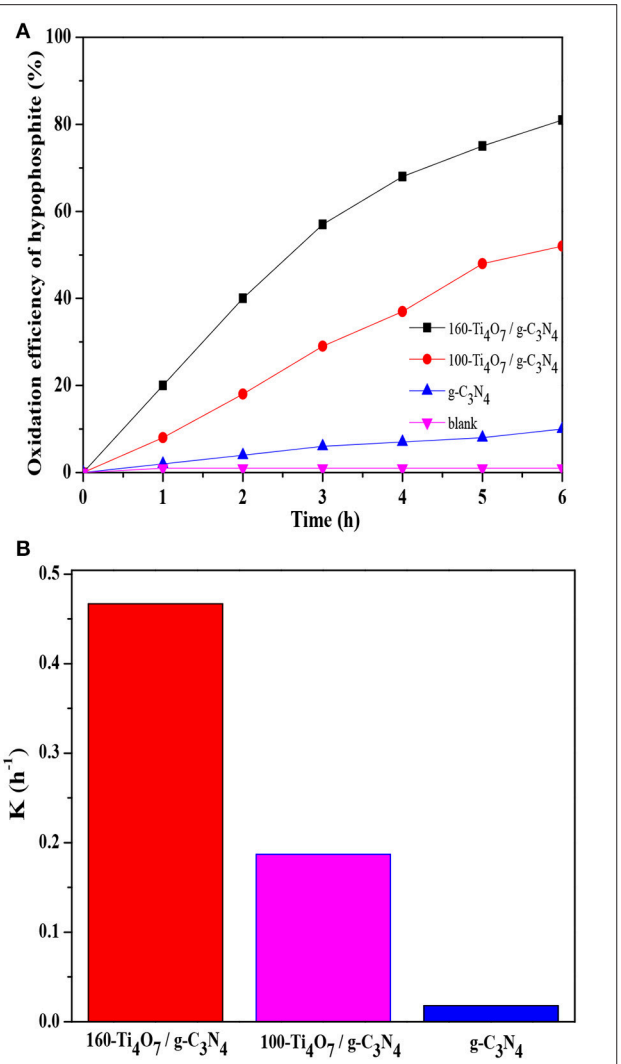

FIGURE 3 | Photocatalytic activity of different photocatalysts. **(A)** The oxidation efficiency of hypophosphite; **(B)** The comparison of oxidation rate constant k.

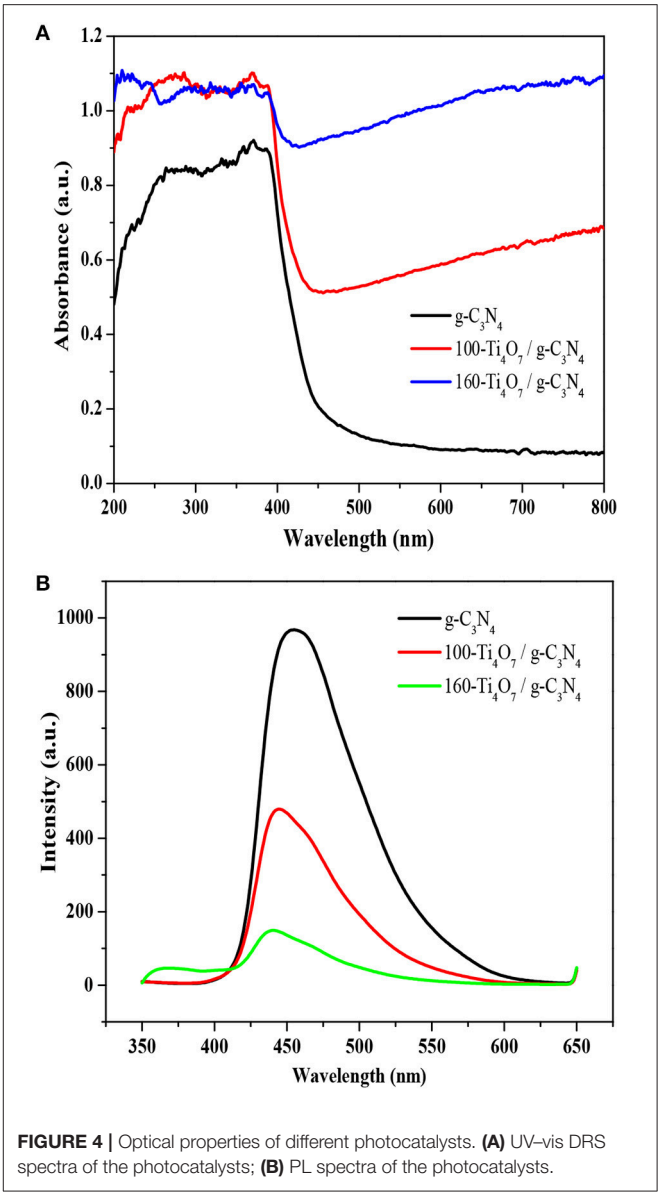

FIGURE 4 | Optical properties of different photocatalysts. **(A)** UV–vis DRS spectra of the photocatalysts; **(B)** PL spectra of the photocatalysts.

in **Figure 2A** that it could be divided into two components including the standard reference carbon (284.8 eV) and the sp^2 bonded C in $N{=}C(-N)_2$ (288.3 eV) (Jo and Natarajan, 2015). The N 1s spectra of $Ti_4O_7/g\text{-}C_3N_4$ could be divided into four peaks as shown in **Figure 2B**. The main peak at 398.7 eV was assigned to sp^2 nitrogen (C=N–C) involved in triazine rings, and the peak at 399.8 eV originated from the tertiary nitrogen bonded to carbon atoms in the form of $N{-}(C)_3$ (Wu et al., 2013). The peak at 401.3 eV was ascribed to amino functions (C–N–H). Another peak centered at 404.4 eV was associated to charging effects or positive charge localization in heterocycles (Gao et al., 2014). These assignments of C 1s and N 1s were agreed well with the XPS results of $g\text{-}C_3N_4$ reported previously. Ti_4O_7 is a mixed-valence compound with two evenly occupied Ti^{4+} ($3d^0$) and Ti^{3+} ($3d^1$) configurations. As shown in **Figure 2C**, two broad peaks at about 458.6 and 464.7 eV were observed, corresponding to the characteristic Ti $2p_{1/2}$ and Ti $2p_{3/2}$ peaks of Ti^{4+}, respectively. Additionally, two peaks at 457.97 and 463.8 eV corresponding to Ti^{3+} also appeared, as reported elsewhere (Zeng et al., 2017). The O 1 s spectra of $Ti_4O_7/g\text{-}C_3N_4$ were shown in **Figure 2D**. The peak with binding energy of 533.5 eV was assigned to the C–O functional groups, and the peaks centered at the binding energies of 531.8 and 529.7 eV were ascribed to the OH–Ti and O–Ti bonds (Li Z. Q. et al., 2017). These results confirmed the presence of Ti_4O_7 on the $g\text{-}C_3N_4$ surface with covalent bonds.

Photocatalytic Activity Analysis

The photocatalytic oxidation of hypophosphite over various samples was analyzed. As shown in **Figure 3A**, the blank experiment indicated that the concentration of hypophosphite

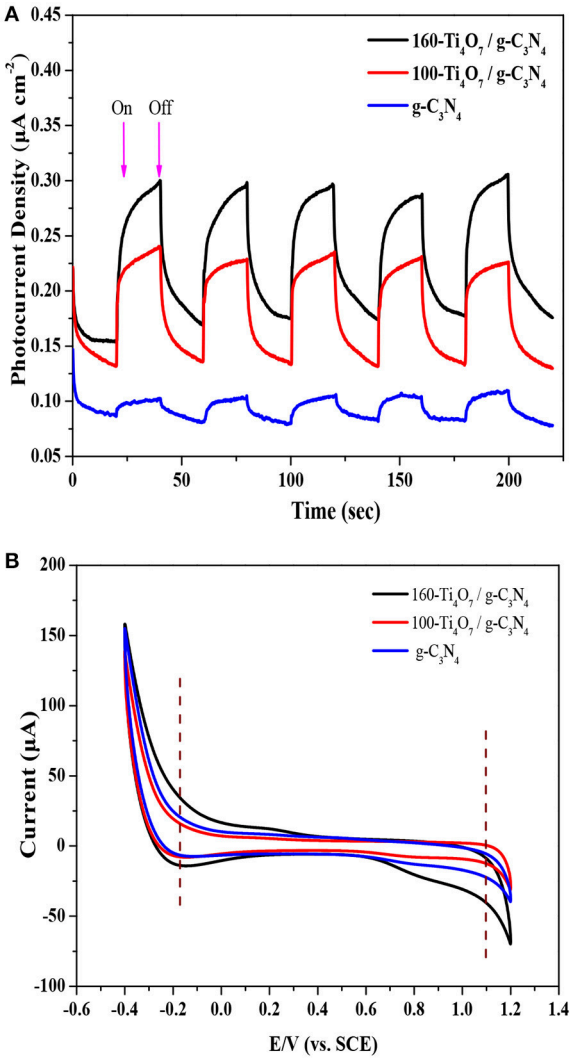

FIGURE 5 | Electrochemical properties analysis of the 160-Ti_4O_7/g-C_3N_4 photocatalyst. **(A)** photocurrent density of different photocatalysts; **(B)** cyclic voltammogram scan of different photocatalysts.

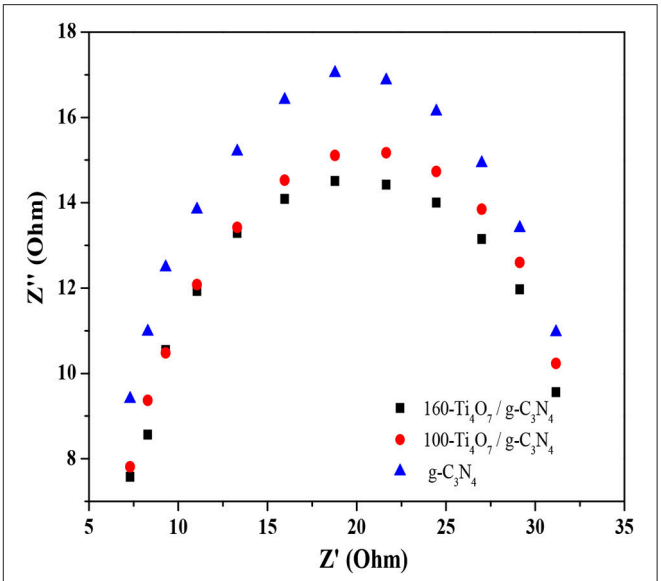

FIGURE 6 | EIS Nyquist plots of the g-C_3N_4, 100-Ti_4O_7/g-C_3N_4, and 160-Ti_4O_7/g-C_3N_4 photocatalysts under visible light irradiation.

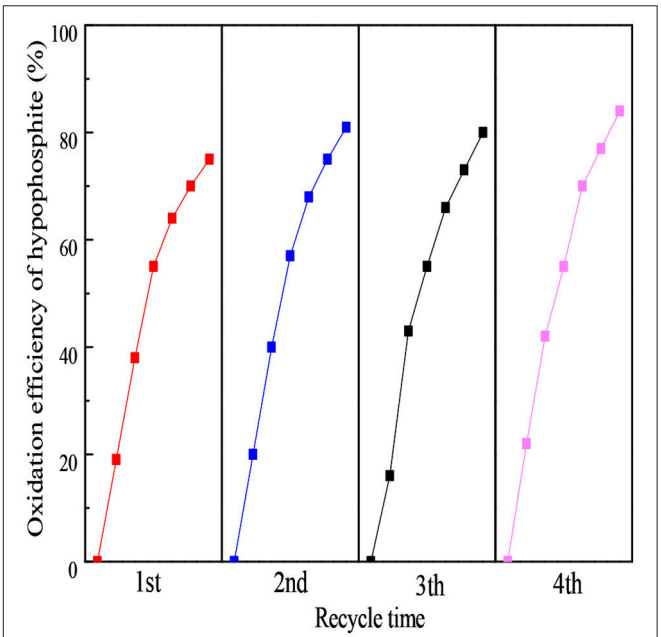

FIGURE 7 | The stability analysis of the 160-Ti_4O_7/g-C_3N_4 photocatalyst under repetitive experiments.

was stable under visible light irradiation ($\lambda > 420$ nm) if there was no photocatalyst presented. Pure g-C_3N_4 showed weak photocatalytic activity with the oxidation efficiency of only 10% possibly owing to the rapid recombination of photo-generated charge carriers and low charge transfer ability (Shi et al., 2017). The 160-Ti_4O_7/g-C_3N_4 photocatalyst had the highest photocatalytic activity with the oxidation efficiency of 81% compared with the pure g-C_3N_4 and 100-Ti_4O_7/g-C_3N_4 photocatalysts.

The photocatalytic oxidation kinetic of the prepared samples was fitted by a pseudo-first-order model, which was depicted by the following Equation (1) (Lu et al., 2018):

$$\ln (C_0/C) = kt \quad (1)$$

Where C_0 and C are the hypophosphite concentrations in solution at times 0 and t, respectively, and k is the first-order rate constant. As shown in **Figure 3B**, the 160-Ti_4O_7/g-C_3N_4 photocatalyst showed the highest photocatalytic oxidation rate of 0.467 h^{-1}, which was 2.5 and 26 times higher than that of 100-Ti_4O_7/g-C_3N_4 and pure g-C_3N_4, respectively. Therefore, the results showed that the 160-Ti_4O_7/g-C_3N_4 photocatalyst

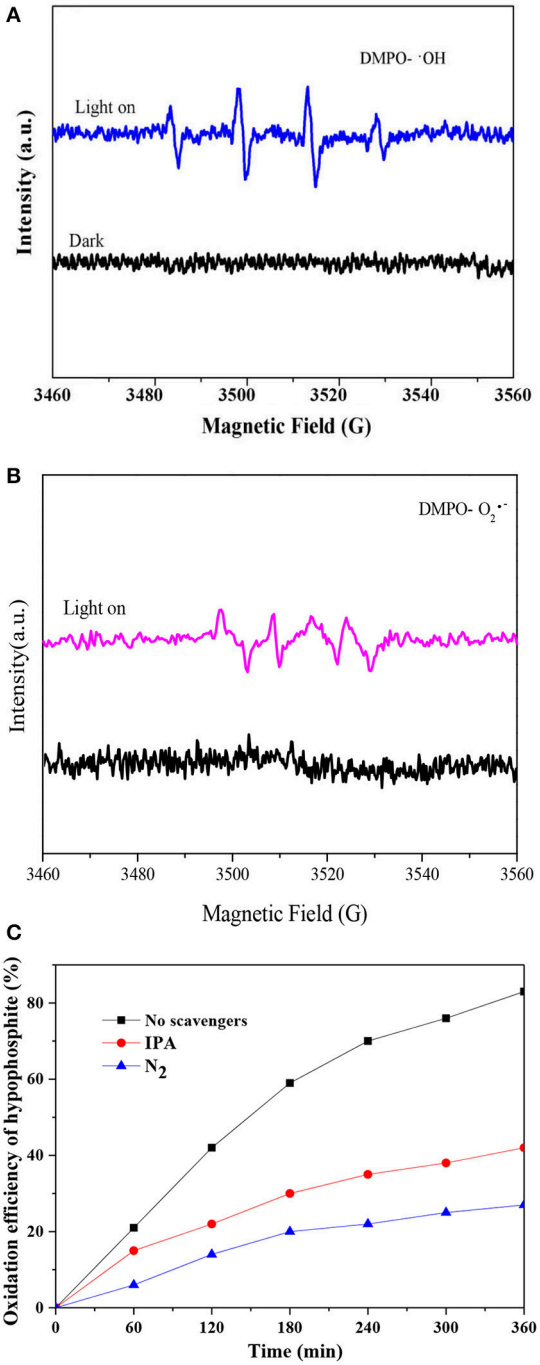

FIGURE 8 | Radials analyses. **(A)** DMPO spin-trapping ESR spectra for ·OH radials analysis; **(B)** DMPO spin-trapping ESR spectra for $\cdot O_2^-$ radials analysis; **(C)** Effect of scavengers on the photocatalytic oxidation process.

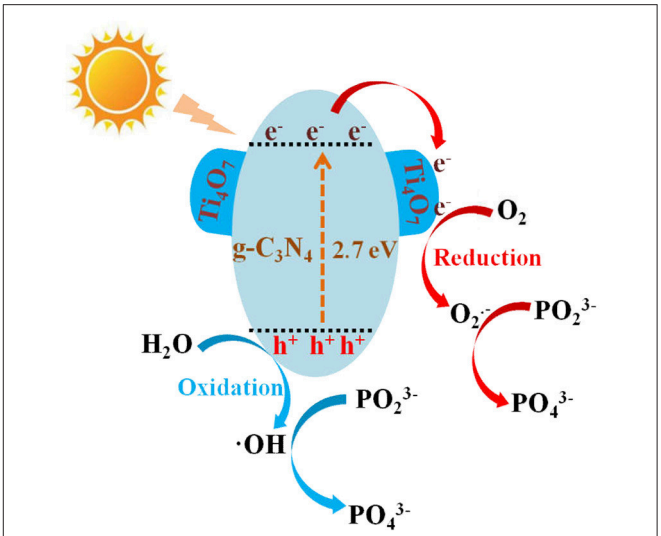

FIGURE 9 | The mechanism of the hypophosphite oxidation over the $Ti_4O_7/g\text{-}C_3N_4$ photocatalyst under visible light irradiation.

exhibited an excellent activity in photocatalytic oxidation of hypophosphite under visible light irritation.

The enhanced photocatalytic activity of $Ti_4O_7/g\text{-}C_3N_4$ and the effect of annealing temperature on $Ti_4O_7/g\text{-}C_3N_4$ photocatalytic activity were further investigated and explained from the perspectives of photoabsorption efficiency, band gap, separation, transformation, and recombination processes of photogenerated carriers in the following sections.

Optical Properties Analysis

The optical properties of $Ti_4O_7/g\text{-}C_3N_4$ and pure $g\text{-}C_3N_4$ photocatalysts were evaluated by UV–vis diffuse reflectance spectra. As shown in **Figure 4A**, the photoabsorption efficiency of $Ti_4O_7/g\text{-}C_3N_4$ was remarkably enhanced compared with the pure $g\text{-}C_3N_4$. The pure $g\text{-}C_3N_4$ held an absorption edge of around 430 nm while the $Ti_4O_7/g\text{-}C_3N_4$ photocatalysts showed a distinct red-shift, indicating that the $Ti_4O_7/g\text{-}C_3N_4$ photocatalysts were more efficient in light harvesting under visible light irradiation. The enhanced photoabsorption efficiency of $Ti_4O_7/g\text{-}C_3N_4$ was due to the narrowed band gap. The band energy gap of the photocatalysts was determined from the formula $\alpha h\nu = A\ (h\nu - E_g)^{n/2}$ (*Eg, α, h, ν, and A* indicate the band gap, optical absorption coefficient, Plank's constant, photonic frequency and a proportionality constant, respectively) (Huang et al., 2017b; Liu et al., 2017a,b; Tian et al., 2017). The band gap calculated from the plot of absorption$^{1/2}$ vs. energy was 2.70, 2.32, and 2.13 eV for $g\text{-}C_3N_4$, $100\text{-}Ti_4O_7/g\text{-}C_3N_4$, and $160\text{-}Ti_4O_7/g\text{-}C_3N_4$, respectively.

Photoluminescence (PL) spectra was used to investigate the separation, transformation and recombination processes of photogenerated carriers. The band–band PL spectrum can directly reflect the separation performance of photo-induced charge carriers, viz. the stronger of the band-band PL signal, the higher of the recombination rate of photo-induced carriers. The PL spectroscopy of the photocatalysts was shown in **Figure 4B**. All photocatalysts exhibited a broad emission peak centered at around 460 nm, which was mainly caused by the recombination of photogenerated electrons and holes produced by $g\text{-}C_3N_4$ (Shi et al., 2017). The PL emission intensity was highest for the pure $g\text{-}C_3N_4$, while the intensity was

significantly lowered for $Ti_4O_7/g\text{-}C_3N_4$. This indicated that the charge carrier recombination was effectively suppressed for the $Ti_4O_7/g\text{-}C_3N_4$ photocatalysts. It is well known that the noble metals, such as Ti_4O_7, are good conductors with excellent electric properties. After formation of noble metals-semiconductors heterostructures, the photogenerated electrons of semiconductors could transfer through these noble metals rapidly and the lifetime of these electrons and holes are prolonged (Cui et al., 2017). In addition, the PL intensity of 160-$Ti_4O_7/g\text{-}C_3N_4$ was much lower than that of 100-$Ti_4O_7/g\text{-}C_3N_4$, indicating that 160-$Ti_4O_7/g\text{-}C_3N_4$ had the effectively decreased charge carrier recombination compared with 100-$Ti_4O_7/g\text{-}C_3N_4$. The higher annealing temperature could etch and tailor $g\text{-}C_3N_4$ with the possibly smaller and thinner nanosheet structure of 160-$Ti_4O_7/g\text{-}C_3N_4$ compared with 100-$Ti_4O_7/g\text{-}C_3N_4$ and thus shortened the distance between the photogenerated electrons and the heterostructure surface, which suppressed the recombination probability of photo-generated electron–hole pairs with the photogenerated electrons rapidly transferring through Ti_4O_7 (Dong et al., 2015).

Electrochemical Properties Analysis

The PC responses of $g\text{-}C_3N_4$, 100-$Ti_4O_7/g\text{-}C_3N_4$, and 160-$Ti_4O_7/g\text{-}C_3N_4$ photocatalysts under visible light irradiation were evaluated to further offer information about the separation and transformation efficiency of photogenerated electrons and holes. As shown in **Figure 5A**, the transient PC responses of all photocatalysts at light on and light off were reversible and stable, and the PC density of 160-$Ti_4O_7/g\text{-}C_3N_4$ was much higher (0.30 $\mu A\ cm^{-2}$) than that of 100-$Ti_4O_7/g\text{-}C_3N_4$ (0.23 $\mu A\ cm^{-2}$) and $g\text{-}C_3N_4$ (0.10 $\mu A\ cm^{-2}$). This indicated that the $Ti_4O_7/g\text{-}C_3N_4$ heterostructures promoted the separation of photogenerated charge carriers (Kang et al., 2016), in line with the PL spectra results as shown in **Figure 4B**. Additionally, this was also supported by the CV test. As shown in **Figure 5B**, a reduction peak at about −0.18 V was observed in $g\text{-}C_3N_4$, 100-$Ti_4O_7/g\text{-}C_3N_4$, and 160-$Ti_4O_7/g\text{-}C_3N_4$, but 160-$Ti_4O_7/g\text{-}C_3N_4$ photocatalyst possessed much higher reduction current, which indicated faster electron transfer in 160-$Ti_4O_7/g\text{-}C_3N_4$ photocatalyst (Samanta and Srivastava, 2017).

Electrochemical impedance spectroscopy was used to investigate the photogenerated charge separation process on the photocatalysts. The radius of the circular arc reflected the resistance of the interfacial charge transfer and separation efficiency of the electron-hole pairs (Leng et al., 2005; Liang and Zhu, 2016). As shown in **Figure 6**, the arc radius decreased gradually when Ti_4O_7 was doped onto the $g\text{-}C_3N_4$ photocatalyst. This meant that the photogenerated charge separation process occurred more easily on $Ti_4O_7/g\text{-}C_3N_4$ compared with the pure $g\text{-}C_3N_4$ because of the decreased energy barrier that the electrode reaction needed to overcome. Moreover, the arc radius of 160-$Ti_4O_7/g\text{-}C_3N_4$ was smaller than that of 100-$Ti_4O_7/g\text{-}C_3N_4$, meaning that the separation of the photogenerated electron–hole pairs was more effective and the interfacial charge transfer of the electron donor/electron acceptor was faster on the 160-$Ti_4O_7/g\text{-}C_3N_4$ photocatalyst.

Catalyst Stability Analysis

The stability was another vital consideration for an excellent photocatalyst. To evaluate the stability of the as-prepared 160-$Ti_4O_7/g\text{-}C_3N_4$ photocatalyst, the repetitive experiments of photocatalytic oxidation of hypophosphite were carried out. As shown in **Figure 7**, the oxidation efficiency of hypophosphite in the four-round continuous reaction tests using 160-$Ti_4O_7/g\text{-}C_3N_4$ photocatalyst was 75, 81, 80, and 84%, respectively. The repetitive experiments results showed that the fabricated $Ti_4O_7/g\text{-}C_3N_4$ photocatalysts had a stable structure possibly with the strong binding force. The N-H groups or conjugated structures in $g\text{-}C_3N_4$ could tightly bond with Ti^{4+} ($3d^0$) and Ti^{3+} ($3d^1$) in Ti_4O_7, which effectively reduced the dissolution of bulk $g\text{-}C_3N_4$ material during the photocatalytic process.

Proposed Mechanism

To clarify the reaction mechanism of photocatalytic oxidation of hypophosphite, the ROS generated under visible light irradiation were analyzed by ESR technique (with DMPO). As shown in **Figure 8A**, no ESR signals were observed in the dark while ·OH was observed under visible light irradiation with four peaks with intensities of 1:2:2:1 attributing to DMPO-·OH generated via a hole oxidative process on H_2O and/or OH^- (Tu et al., 2017). Moreover, $\cdot O_2^-$ was also observed under visible light irradiation with a four-line spectrum with the relative intensities of 1:1:1:1 assigned to DMPO-$\cdot O_2^-$ adduct derived from O_2 reduction by electrons (Huang et al., 2015), however, no ESR signals were observed in the dark as shown in **Figure 8B**. Therefore, both ·OH and $\cdot O_2^-$ would contribute to the photocatalytic oxidation of hypophosphite and their contributions were further investigated with and without radical scavengers. Isopropanol (IPA) and N_2 purging were applied with IPA acting as the ·OH radicals quencher and N_2 purging reducing the superoxide $\cdot O_2^-$ radicals (Yang et al., 2016). As shown in **Figure 8C**, the photocatalytic oxidation efficiency of hypophosphite decreased from 83% (without radical scavengers) to 42% (with IPA) and even 27% (with N_2 purging). These results confirmed that both ·OH and $O_2\cdot^-$ radicals were the major active radical species for hypophosphite oxidation in the photocatalytic process with $O_2\cdot^-$ accounting for a more significant contribution. Note that the photocatalytic oxidation efficiency of hypophosphite did not decrease to zero with the lowest efficiency of 27% in the presence of N_2 purging, indicating that holes and some other radicals may also contribute to the photocatalytic oxidation process to some extent. It was reported that reactive oxygen species (ROS), such as superoxide ($\cdot O_2^-$), hydroxyl radicals (·OH), singlet oxygen ($^1O_2$), peroxyl ($RO_2\cdot$), and alkoxyl (RO-) as well as hypochlorous acid (HOCl) are basically produced in the photocatalytic process (Huang et al., 2017a), which may also contribute to the photocatalytic oxidation of hypophosphite in this case.

According to the above results and those reported in the literature, the possible photocatalytic mechanism of $Ti_4O_7/g\text{-}C_3N_4$ on hypophosphite oxidation was illustrated in **Figure 9**.

The possible photocatalytic processes were as follows:

$$Ti_4O_7/g\text{-}C_3N_4 + h\nu \rightarrow g\text{-}C_3N_4(e^- + h^+) \quad (2)$$

$$g\text{-}C_3N_4\ (e^-) + Ti_4O_7 \rightarrow Ti_4O_7\ (e^-) \quad (3)$$

$$Ti_4O_7 + h\nu \rightarrow Ti_4O_7\ (e^-) \quad (4)$$

$$Ti_4O_7\ (e^-) + O_2 \rightarrow \cdot O_2^- \quad (5)$$

$$\cdot O_2^- + PO_2^{3-} \rightarrow PO_4^{3-} \quad (6)$$

$$g\text{-}C_3N_4\ (h^+) + OH^- \rightarrow \cdot OH \quad (7)$$

$$\cdot OH + PO_2^{3-} \rightarrow PO_4^{3-} \quad (8)$$

$$g\text{-}C_3N_4\ (h^+) + PO_2^{3-} \rightarrow PO_4^{3-} \quad (9)$$

Firstly, the electrons (e^-) in valence band of $g\text{-}C_3N_4$ under visible light irradiation could be excited to the conduction band, leaving the holes (h^+) in valence band of $g\text{-}C_3N_4$ (Equation 2). Then the photogenerated electrons in the conduction band of $g\text{-}C_3N_4$ would continually transfer to Ti_4O_7 until the same Fermi levels reached (Equation 3). Thus, the photogenerated electrons and holes were located at Ti_4O_7 and $g\text{-}C_3N_4$, respectively, leading to the effective separation of the photoinduced charge carriers. Furthermore, the electrons might be also generated from the Ti_4O_7 particles (Equation 4) with the product easily reacting with the adsorbed oxygen molecules to produce $\cdot O_2^-$ (Equation 5) followed by the oxidation of hypophosphite to phosphate (Equation 6). Meanwhile, the photogenerated holes as the strong oxidants could oxidize OH^- to ·OH radicals, and then the hypophosphite was directly oxidized to phosphate (Equations 7 and 8). In addition, some photogenerated holes could directly oxidize hypophosphite to phosphate (Equation 9).

CONCLUSION

The enhancement of $Ti_4O_7/g\text{-}C_3N_4$ visible light photocatalytic performance on hypophosphite oxidation and the effect of annealing temperature and the corresponding mechanism were investigated in this study. 160-$Ti_4O_7/g\text{-}C_3N_4$ (fabricated at 160°C) photocatalyst showed the highest oxidation efficiency of hypophosphite of 81% and the highest photocatalytic oxidation rate of 0.467 h^{-1} comparing with 100-$Ti_4O_7/g\text{-}C_3N_4$ (fabricated at 100°C) and pure $g\text{-}C_3N_4$. The enhanced photocatalytic performance of 160-$Ti_4O_7/g\text{-}C_3N_4$ could be ascribed to the effective charge separation and enhanced photoabsorption efficiency. Additionally, ESR results showed that hydroxyl radicals and superoxide anion radicals were mainly responsible to the oxidation of hypophosphite with $O_2\cdot^-$ accounting for a more significant contribution. Moreover, $Ti_4O_7/g\text{-}C_3N_4$ photocatalysts showed the remarkable stability in the repetitive experiments. Our work demonstrated that the rational design and construction of isotype heterojunction was an effective strategy to develop the efficient photocatalysts under visible light irradiation.

AUTHOR CONTRIBUTIONS

All authors listed have made a substantial, direct and intellectual contribution to the work, and approved it for publication.

FUNDING

This work was supported by National Natural Science Foundation of China (No. 51608086); Science and Technology Project from Chongqing (CSTC2015JCYJA20027); Scientific and Technological Research Program of Chongqing Municipal Education Commission (KJ1501103); Chongqing Key Laboratory of Environmental Materials and Remediation Technology, Chongqing University of Arts and Sciences (CKE1407); Natural Science Foundation of Yongchuan, Chongqing (Ycstc, 2014ac4001); Scientific Research Foundation of Chongqing University of Arts and Sciences (R2014CH08).

REFERENCES

Bulasara, V. K., Thakuria, H., Uppaluri, R., and Purkait, M. K. (2011). Effect of process parameters on electroless plating and nickel-ceramic composite membrane characteristics. *Desalination* 268, 195–203. doi: 10.1016/j.desal.2010.10.025

Cao, X. C., Sun, Z. H., Zheng, X. J., Tian, J. H., Jin, C., Yang, R. Z., et al. (2017). $MnCo_2O_4$ decorated Magnéli phase titanium oxide as a carbon-free cathode for Li–O_2 batteries. *J. Mater. Chem. A* 5, 19991–19996. doi: 10.1039/c7ta06152h

Chisaka, M., Ando, Y., Yamamoto, Y., and Itagaki, N. (2016). A carbon-support-free titanium oxynitride catalyst for proton exchange membrane fuel cell cathodes. *Electrochim. Acta* 214, 165–172. doi: 10.1016/j.electacta.2016.08.032

Cui, W., Li, J. Y., Cen, W. L., Sun, Y. J., Lee, S. C., and Dong, F. (2017). Steering the interlayer energy barrier and charge flow via bioriented transportation channels in $g\text{-}C_3N_4$: enhanced photocatalysis and reaction mechanism. *J. Catal.* 352, 351–360. doi: 10.1016/j.jcat.2017.05.017

Dong, F., Li, Y. H., Wang, Z. Y., and Ho, W. K. (2015). Enhanced visible light photocatalytic activity and oxidation ability of porous graphene-like $g\text{-}C_3N_4$ nanosheets via thermal exfoliation. *Appl. Surf. Sci.* 358, 393–403. doi: 10.1016/j.apsusc.2015.04.034

Gao, D. Q., Xu, Q., Zhang, J., Yang, Z. L., Si, M. S., Yan, Z. J., et al. (2014). Defect-related ferromagnetism in ultrathin metal-free C_3N_4 nanosheets. *Nanoscale* 6, 2577–2581. doi: 10.1039/c3nr04743a

Ge, C., Chai, Y., Wang, H., and Kan, M. (2017). Ocean acidification: one potential driver of phosphorus eutrophication. *Mar. Pollut. Bull.* 115, 149–153. doi: 10.1016/j.marpolbul.2016.12.016

Guo, L., Jing, Y., and Chaplin, B. P. (2016). Development and characterization of ultrafiltration TiO_2 magnéli phase reactive electrochemical membranes. *Environ. Sci. Technol.* 50, 1428–1436. doi: 10.1021/acs.est.5b04366

Huang, H., Han, X., Li, X., Wang, S., Chu, P., and Zhang, Y. (2015). Fabrication of multiple heterojunctions with tunable visible-light-active photocatalytic reactivity in BiOBr–BiOI full-range composites based on microstructure modulation and band structures. *ACS Appl. Mater. Interfaces* 7, 482–492. doi: 10.1021/am5065409

Huang, H., Tu, S., Zeng, C., Zhang, T., Reshak, A., and Zhang, Y. H. (2017a). Macroscopic polarization enhancement promoting photo- and piezoelectric-induced charge separation and molecular oxygen activation. *Angew. Chem. Int. Edn.* 56, 11860–11864. doi: 10.1002/anie.201706549

Huang, H. W., Xiao, K., Tian, N., Dong, F., Zhang, T. R., Du, X., et al. (2017b). Template-free precursor-surface-etching route to porous, thin $g\text{-}C_3N_4$ nanosheets for enhancing photocatalytic reduction and oxidation activity. *J. Mater. Chem. A* 5, 17452–17463. doi: 10.1039/c7ta04639a

Jo, W. K., and Natarajan, T. S. (2015). Influence of TiO_2 morphology on the photocatalytic efficiency of direct Z-scheme $g\text{-}C_3N_4/TiO_2$ photocatalysts for isoniazid degradation. *Chem. Eng. J.* 281, 549–565. doi: 10.1016/j.cej.2015.06.120

Jourshabani, M., Shariatinia, Z., and Badiei, A. (2017). Facile one-pot synthesis of cerium oxide/sulfur-doped graphitic carbon nitride (g-C_3N_4) as efficient nanophotocatalysts under visible light irradiation. *J. Colloid Interface Sci.* 507, 59–73. doi: 10.1016/j.jcis.2017.07.106

Kang, K., Watanabe, S., Broch, K., Sepe, A., Brown, A., Nasrallah, I., et al. (2016). 2D coherent charge transport in highly ordered conducting polymers doped by solid state diffusion. *Nat. Mater.* 15, 896–902. doi: 10.1038/NMAT4634

Kolbrecka, K., and Przyluski, J. (1994). Sub-stoichiometric titanium oxides as ceramic electrodes for oxygen evolution—structural aspects of the voltammetric behaviour of Ti_nO_{2n-1}. *Electrochim. Acta* 39, 1591–1595. doi: 10.1016/0013-4686(94)85140-9

Leng, W. H., Zhang, Z., Zhang, J. Q., and Cao, C. N. (2005). Investigation of the kinetics of a TiO_2 photoelectrocatalytic reaction involving charge transfer and recombination through surface states by electrochemical impedance spectroscopy. *J. Phys. Chem. B* 109, 15008–15023. doi: 10.1021/jp051821z

Li, J. D., Zhang, X. L., Raziq, F., Wang, J. S., Liu, C., Liu, Y. D., et al. (2017). Improved photocatalytic activities of g-C_3N_4 nanosheets by effectively trapping holes with halogen-induced surface polarization and 2,4-dichlorophenol decomposition mechanism. *Appl. Catal. B Environ.* 218, 60–67. doi: 10.1016/j.apcatb.2017.06.038

Li, L. Y., Takahashi, N., Kaneko, K., Shimizu, T., and Takarada, T. (2015). A novel method for nickel recovery and phosphorus removal from spent electroless nickel-plating solution. *Sep. Purif. Technol.* 147, 237–244. doi: 10.1016/j.seppur.2015.04.029

Li, X. X., Zhu, A. L., Qu, W., Wang, H. J., Hui, R., Zhang, L., et al. (2010). Magneli phase Ti_4O_7 electrode for oxygen reduction reaction and its implication for zinc-air rechargeable batteries. *Electrochim. Acta* 55, 5891–5898. doi: 10.1016/j.electacta.2010.05.041

Li, Z. Q., Qi, M. Y., Tu, C. Y., Wang, W. P., Chen, J. R., and Wang, A. J. (2017). Highly efficient removal of chlorotetracycline from aqueous solution using graphene oxide/TiO_2 composite: properties and mechanism. *Appl. Surf. Sci.* 425, 765–775. doi: 10.1016/j.apsusc.2017.07.027

Liang, F. F., and Zhu, Y. F. (2016). Enhancement of mineralization ability for phenol via synergetic effect of photoelectrocatalysis of g-C_3N_4 film. *Appl. Catal. B Environ.* 180, 324–329. doi: 10.1016/j.apcatb.2015.05.009

Lin, F., Shao, B., Li, Z., Zhang, J. Y., Wang, H., Zhang, S. H., et al. (2017). Visible light photocatalysis over solid acid: enhanced by gold plasmonic effect. *Appl. Catal. B Environ.* 218, 480–487. doi: 10.1016/j.apcatb.2017.06.076

Liu, C. Y., Huang, H. W., Ye, L. Q., Yu, S. X., Tian, N., Du, X., et al. (2017a). Intermediate-mediated strategy to horn-like hollow mesoporous ultrathin g-C_3N_4 tube with spatial anisotropic charge separation for superior photocatalytic H_2 evolution. *Nano Energy* 41, 738–748. doi: 10.1016/j.nanoen.2017.10.031

Liu, C. Y., Zhang, Y. H., Dong, F., Reshak, A. H., Ye, L. Q., Pinna, N., et al. (2017b). Chlorine intercalation in graphitic carbon nitride for efficient photocatalysis. *Appl. Catal. B Environ.* 203, 465–474. doi: 10.1016/j.apcatb.2016.10.002

Lu, X. J., Wang, Y., Zhang, X. Y., Xu, G. Q., Wang, D. M., Lv, J., et al. (2018). NiS and MoS_2 nanosheet co-modified graphitic C_3N_4 ternary heterostructure for high efficient visible light photodegradation of antibiotic. *J. Hazard. Mater.* 341, 10–19. doi: 10.1016/j.jhazmat.2017.07.004

Maragatha, J., Rani, C., Rajendran, S., and Karuppuchamy, S. (2017). Microwave synthesis of nitrogen doped Ti_4O_7 for photocatalytic applications. *Physica E* 93, 78–82. doi: 10.1016/j.physe.2017.05.020

McDowell, M. M., Ivey, M. M., Lee, M. E., Firpo, V. V., Salmassi, T. M., Khachikian, C. S., et al. (2004). Detection of hypophosphite, phosphite, and orthophosphate in natural geothermal water by ion chromatography. *J. Chromatogr. A* 1039, 105–111. doi: 10.1016/j.chroma.2003.11.056

Montangero, A., and Belevi, H. (2007). Assessing nutrient flows in septic tanks by eliciting expert judgement: a promising method in the context of developing countries. *Water Res.* 41, 1052–1064. doi: 10.1016/j.watres.2006.10.036

Noman, M. T., Wiener, J., Saskova, J., Ashraf, M. A., Vikova, M., Jamshaid, H., et al. (2018). *In-situ* development of highly photocatalytic multifunctional nanocomposites by ultrasonic acoustic method. *Ultrason. Sonochem.* 40, 41–56. doi: 10.1016/j.ultsonch.2017.06.026

Oturan, N., Ganiyu, S. O., Raffy, S., and Oturan, M. A. (2017). Sub-stoichiometric titanium oxide as a new anode material for electro-Fenton process: application to electrocatalytic destruction of antibiotic amoxicillin. *Appl. Catal. B Environ.* 217, 214–223. doi: 10.1016/j.apcatb.2017.05.062

Samanta, S., and Srivastava, R. (2017). Thermal catalysis vs. photocatalysis: a case study with $FeVO_4$/g-C_3N_4 nanocomposites for the efficient activation of aromatic and benzylic C–H bonds to oxygenated products. *Appl. Catal. B Environ.* 218, 621–636. doi: 10.1016/j.apcatb.2017.06.043

Shao, H. X., Zhao, X., Wang, Y. B., Mao, R., Wang, Y., Qiao, M., et al. (2017). Synergetic activation of peroxymonosulfate by Co_3O_4 modified g-C_3N_4 for enhanced degradation of diclofenac sodium under visible light irradiation. *Appl. Catal. B Environ.* 218, 810–818. doi: 10.1016/j.apcatb.2017.07.016

Shi, A. Y., Li, H. H., Yin, S., Liu, B., Zhang, J. C., and Wang, Y. H. (2017). Effect of conjugation degree and delocalized π-system on the photocatalytic activity of single layer g-C_3N_4. *Appl. Catal. B Environ.* 218, 137–146. doi: 10.1016/j.apcatb.2017.06.017

Sun, S. P., Liao, X. M., Yin, G. F., Yao, Y. D., Huang, Z. B., and Pu, X. M. (2016). Enhanced electrochemical performance of TiO_2 nanotube array electrodes by controlling the introduction of substoichiometric titanium oxides. *J. Alloy. Compd.* 680, 538–543. doi: 10.1016/j.jallcom.2016.04.171

Sun, X., Jiang, D., Zhang, L., and Wang, W. Z. (2018). Alkaline modified g-C_3N_4 photocatalyst for high selective oxide coupling of benzyl alcohol to benzoin. *Appl. Catal. B Environ.* 220, 553–560. doi: 10.1016/j.apcatb.2017.08.057

Takeda, I., Somura, H., and Mori, Y. (2010). Recovery of phosphorus from natural water bodies using iron-oxidizing bacteria and woody biomass. *Ecol. Eng.* 36, 1064–1069. doi: 10.1016/j.ecoleng.2010.04.019

Teng, W., Wang, Y. M., Huang, H. H., Li, X. Y., and Tang, Y. B. (2017). Enhanced photoelectrochemical performance of MoS_2 nanobelts-loaded TiO_2 nanotube arrays by photo-assisted electrodeposition. *Appl. Surf. Sci.* 425, 507–517. doi: 10.1016/j.apsusc.2017.06.297

Tian, N., Zhang, Y. H., Li, X. W., Xiao, K., Du, X., Dong, F., et al. (2017). Precursor-reforming protocol to 3D mesoporous g-C_3N_4 established by ultrathin self-doped nanosheets for superior hydrogen evolution. *Nano Energy* 38, 72–81. doi: 10.1016/j.nanoen.2017.05.038

Tian, S. C., Li, Y. B., and Zhao, X. (2015). Cyanide removal with a copper/active carbon fiber cathode via a combined oxidation of a Fenton-like reaction and *in situ* generated copper oxides at anode. *Electrochim. Acta* 180, 746–755. doi: 10.1016/j.electacta.2015.09.006

Tu, S. C., Huang, H. W., Zhang, T. R., and Zhang, Y. H. (2017). Controllable synthesis of multi-responsive ferroelectric layered perovskite-like $Bi_4Ti_3O_{12}$: photocatalysis and piezoelectric-catalysis and mechanism insight. *Appl. Catal. B Environ.* 219, 550–562. doi: 10.1016/j.apcatb.2017.08.001

Wang, D., Chen, N., Yu, Y., Hu, W. W., and Feng, C. P. (2016). Investigation on the adsorption of phosphorus by Fe-loaded ceramic adsorbent. *J. Colloid Interface Sci.* 464, 277–284. doi: 10.1016/j.jcis.2015.11.039

Wang, W., Fang, J. J., Shao, S. F., Lai, M., and Lu, C. H. (2017). Compact and uniform TiO_2@g-C_3N_4 core-shell quantum heterojunction for photocatalytic degradation of tetracycline antibiotics. *Appl. Catal. B Environ.* 217, 57–64. doi: 10.1016/j.apcatb.2017.05.037

Wu, G. S., Thind, S. S., Wen, J. L., Yan, K., and Chen, A. C. (2013). A novel nanoporous α-C_3N_4 photocatalyst with superior high visible light activity. *Appl. Catal. B Environ.* 142–143, 590–597. doi: 10.1016/j.apcatb.2013.05.070

Yang, X. L., Qian, F. F., Zou, G. J., Li, M. L., Lu, J. R., Li, Y. M., et al. (2016). Facile fabrication of acidified g-C_3N_4/g-C_3N_4 hybrids with enhanced photocatalysis performance under visible light irradiation. *Appl. Catal. B Environ.* 193, 22–35. doi: 10.1016/j.apcatb.2016.03.060

Ye, Y. Y., Ngo, H. H., Guo, W. S., Liu, Y. W., Li, J. X., Liu, Y., et al. (2017). Insight into chemical phosphate recovery from municipal wastewater. *Sci. Total Environ.* 576, 159–171. doi: 10.1016/j.scitotenv.2016.10.078

Ye, Z. L., Deng, Y. Y., Lou, Y. Y., Ye, X., Zhang, J. Q., and Chen, S. H. (2017). Adsorption behavior of tetracyclines by struvite particles in the process of phosphorus recovery from synthetic swine wastewater. *Chem. Eng. J.* 313, 1633–1638. doi: 10.1016/j.cej.2016.11.062

You, S. J., Liu, B., Gao, Y. F., Wang, Y., Tang, C. Y. Y., Huang, Y. B., et al. (2016). Monolithic porous magnéli-phase Ti_4O_7 for electro-oxidation treatment of industrial wastewater. *Electrochim. Acta* 214, 326–335. doi: 10.1016/j.electacta.2016.08.037

Zeng, X. K., Wang, Z. Y., Wang, G., Gengenbach, T. R., McCarthy, D. T., Deletic, A., et al. (2017). Highly dispersed TiO_2 nanocrystals and WO_3 nanorods on reduced graphene oxide: Z-scheme photocatalysis system for accelerated photocatalytic water disinfection. *Appl. Catal. B Environ.* 218, 163–173. doi: 10.1016/j.apcatb.2017.06.055

Zhang, J. S., Zhang, G. G., Chen, X. F., Lin, S., Möhlmann, L., Dołega, G., et al. (2012a). Co-monomer control of carbon nitride semiconductors to optimize hydrogen evolution with visible light. *Angew. Chem. Int. Ed.* 124, 3237–3241. doi: 10.1002/anie.201106656

Zhang, J. S., Zhang, M. W., Zhang, G. G., and Wang, X. C. (2012b). Synthesis of carbon nitride semiconductors in sulfur flux for water photoredox catalysis. *ACS Catal.* 2, 940–948. doi: 10.1021/cs300167b

Conflict of Interest Statement: Author LY was employed by company of Heibei Yinfa Meifute Environmental Engineering Co., Ltd.

The other authors declare that the research was conducted in the absence of any commercial or financial relationships that could be construed as a potential conflict of interest.